

A microfluidic platform to study carbon dioxide dissolution and solubility in physical solvents

Milad Abolhasani,^{*a} Mayank Singh^a, Eugenia Kumacheva^{b,c}, and Axel Günther^{a,c}

^a Department of Mechanical and Industrial Engineering, University of Toronto, Toronto, ON, M5S 3G8, Canada. E-mail: axel.guenther@utoronto.ca

^b Department of Chemistry, University of Toronto, Toronto, ON, M5S 3H6, Canada. E-mail: ekumache@chem.utoronto.ca

^c Institute of Biomaterials & Biomedical Engineering, University of Toronto, 164 College Street, Toronto, Ontario, M5S 3G9, Canada.

S1 Liquid film calculations

At low capillary numbers considered here, $Ca < 10^{-2}$, the liquid film thickness at the walls, δ_{fw} , and at the corners, δ_{fc} , of the microchannel (Fig.S1a), is only a function of the channel hydrodynamic diameter, d_h , according to the experimental results of Kolb and Cerro¹ and Fries *et al.*²:

$$\delta_{fw} = 0.02 \times d_h = 0.02 \times 300 \mu\text{m} = 6 \mu\text{m}, \quad \delta_{fc} = 0.1 \times d_h = 0.12 \times 300 \mu\text{m} = 36 \mu\text{m} \quad (1)$$

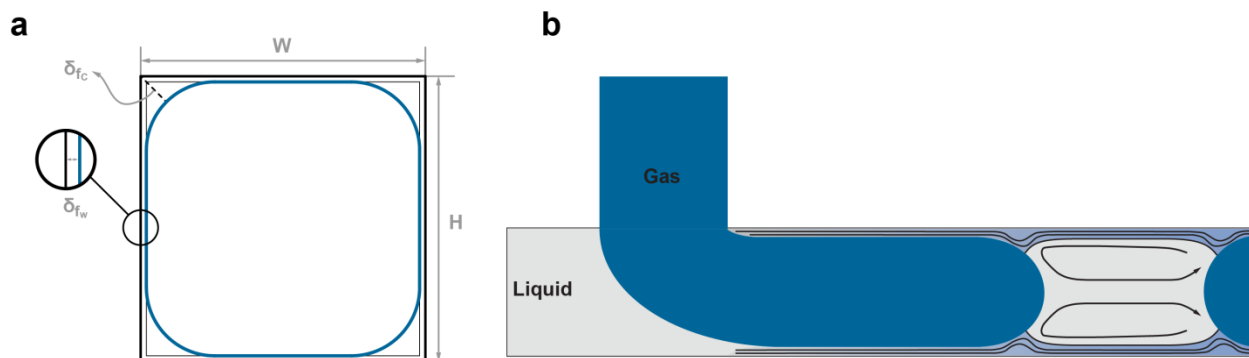


Fig. S1 (a) Cross-sectional view of a gas plug moving in a microchannel. The liquid films at the walls and corners are illustrated. (b) Gas plug break-up and streamlines of the liquid films surrounding the gas plugs are schematically shown.

For the liquid film thicknesses, the cross-sectional areas associated with the films at the side walls and corners are $3456 \mu\text{m}^2$ and $8050 \mu\text{m}^2$, respectively. The amount of liquid at the corners is 2.33 times larger as compared to the side wall regions. Considering a 5 mm long gas plug, the cumulative liquid volume (prior to dissolution taking place) associated with both film regions is $5.06 \times 10^{-8} \text{L}$, a volume that is approximately equal to the liquid slug volume, $V_s = 5.85 \times 10^{-8} \text{L}$. As a result of this analysis, we expect the liquid content of the films regions to become saturated right at the location where bubble formation occurs. The (remaining) gas-liquid mass transfer is therefore practically taking place through the plug cap regions only. To support this claim, the saturation times/lengths for the both films at the walls and corners were calculated assuming only diffusive transport in the films. The diffusion coefficient of carbon dioxide in DMC, $D_{CO_2,DMC}$, was estimated using a relationship suggested by Versteeg and Swaaij,^{3,4}

$$D_{CO_2,DMC} = D_{CO_2,Water} \times \left(\frac{\mu_{Water}(T)}{\mu_{DMC}(T)} \right)^{0.8} = 2.75 \times 10^{-9} \left(\frac{\text{m}^2}{\text{s}} \right) \quad (2)$$

where $D_{CO_2,Water}$ is the diffusion coefficient of carbon dioxide molecules in water at the same temperature as the CO_2 – DMC mixture, $\mu_{DMC}(T) = 0.598 \times 10^{-3} \text{ (Pa}\cdot\text{s)}$ ⁵ and $\mu_{Water}(T) = 1.94 \times 10^{-9} \text{ (m}^2/\text{s)}$ ⁶ are the viscosities of the working fluids at the temperature $T = 298 \text{K}$.

Using Eqs. (1) and (2), diffusion times associated with the liquid films, $t_{D,w}$, and the corners, $t_{D,c}$, can be calculated as:

$$t_{D,w} = \frac{(\delta_{fW})^2}{D_{CO_2,DMC}}, \quad t_{D,c} = \frac{(\delta_{fC})^2}{D_{CO_2,DMC}} \quad (3)$$

The diffusion times required to saturate the liquid films at the walls and corners are 0.013 s and 0.32 s, respectively. Diffusion times can be converted into length scales by multiplying with U_B . The saturation length for the liquid film at the walls and corners are 0.26 mm and 6.4 mm, respectively. Therefore, for a 5 mm long gas plug, the liquid films at the walls and corners will be saturated while the gas plug break-up occurs. As shown in Fig. S1a, the liquid within the saturated film regions follows the illustrated streamlines and stays within the liquid film boundaries. Consequently, the mass transfer in the liquid film sections can be neglected and it can be assumed that the mass transfer exclusively takes place at the plug caps.

S2 Plug and liquid slug volume calculations

After the plug and the liquid slug lengths have been determined from image processing at six different positions X along the flow channel (Fig. S2), the plug and the liquid slug volumes, $(V_B)_{D,P}$ and V_S , were evaluated using the following equations:

$$(V_B)_{D,P}(X) = H \cdot w [L_B(X) - (H - 2\delta_f)] + w \cdot \pi(H - 2\delta_f)^2 \quad (4)$$

$$V_S = H \cdot w \cdot L_S + \left[H \cdot w(H - 2\delta_f) - \frac{4}{3} \pi \left(\frac{H}{2} - \delta_f \right)^2 \right] \quad (5)$$

where δ_f is the thickness of the liquid film surrounding the plug, H is the channel height and w is the channel width.

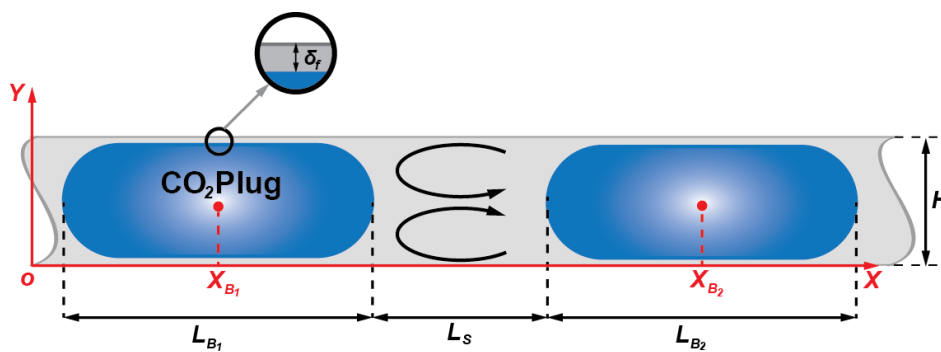


Fig. S2 Schematic of the plug length, the liquid slug length and the liquid film thickness in a microchannel.

S3 Parameter space associated with initial flow conditions

The automated microfluidic system was utilized to systematically investigate how the initial plug length, the initial slug length and the initial plug velocity of different gas-liquid pairs can be interrelated for a given liquid flow rate and gas inlet pressure. The obtained results are summarized in Fig. S3.

Inverse of liquid volume fraction, $(Q_G+Q_L)/Q_L$, the inverse of gas volume fraction, $(Q_G+Q_L)/Q_G$, and the total gas and liquid superficial velocities, j_L+j_G characterize the initial working space of a gas-liquid segmented flow.^{7, 8} At each experimental condition, i.e. for a fixed Q_L and P_G , the gas flow rate was measured using the method described in the paper. As shown in Fig. S3a-c, L_{B0} , L_{S0} and U_{B0} were linearly related to the inverse of liquid and gas volume fractions and total liquid and gas superficial velocities (Eq. 6). The resulting lines from the curve fittings of the experimental data were used to find the initial working space of the system (Fig. S3d).

$$\frac{L_{B0}}{w} = 2.45 \left(\frac{j_G + j_L}{j_L} \right) - 1.69, \quad \frac{L_{S0}}{w} = 5.95 \left(\frac{j_G + j_L}{j_G} \right) - 5.14, \quad U_{B0} = 1.07(j_L + j_G) - 5.68 \text{ (mm/s)} \quad (6)$$

The resulting working surface of our segmented flow system for the case of nitrogen and ethanol was:

$$\frac{\frac{L_{B0}}{W} + 1.69}{2.45} = \frac{\frac{L_{S0}}{W} + 5.14}{\frac{L_{S0}}{W} - 0.81}}{W} = \frac{U_{B0} + 5.68\left(\frac{mm}{s}\right)}{1.07j_L} \quad (7)$$

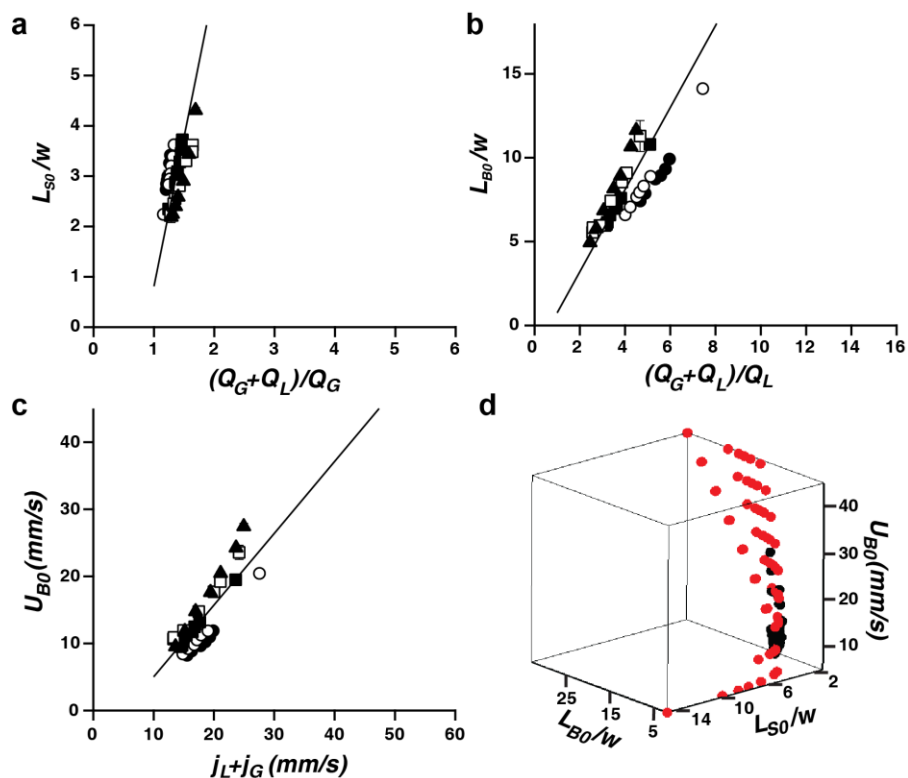


Fig. S3 (a) Variation of the non-dimensionalized initial slug length as a function of the inverted volume fraction of the gas phase for different gas and liquid superficial velocities. (b) Variation of the initial plug length versus the inverse of the liquid volume fraction. (c) Variation of the initial plug velocity as a function of the gas superficial velocity and the liquid superficial velocity. (d) The initial working plane of the segmented flow. Red color: 3D scatter data of the calculated plane using the gas and liquid volume fractions. Black color: scatter plot of the measured data points. The working fluids are nitrogen and ethanol.

Figure S3(d) suggests that the surface corresponding to Eq. (7) represents all measured data points well. We use the obtained parameter space related to the conditions at the inlet of the segmented flow channel, X_0 , to systematically study the effects of the different inter-related parameters, e.g., the plug length, the slug length and the plug velocity. Using the above mentioned initial working space, the dynamically adjusted segmented flow parameters, L_{B0} , L_{S0} and U_{B0} can be maintained constant separately.

S4 Numerical simulation of the temperature distribution inside the microchannel

To determine the temperature distribution along the flow direction a three-dimensional numerical simulation using a commercial multiphysics program (Comsol, version 4.2, COMSOL Inc., Burlington, MA) was conducted assuming a single phase flow of the physical solvent (DMC) inside the silicon microfluidic device. Figure S4 shows the two-dimensional temperature distribution across the device. An unstructured mesh was generated with the resolution of the narrowest region of 5 elements, resulting in 5,860,889 elements. Convective heat losses were considered at all outer surfaces of the microreactor (i.e. external natural convection for bottom of the silicon, top of the Borofloat layer and the side walls). The following boundary conditions were imposed: Temperatures of the heating element and inlet of DMC were assumed to be 320K and 298 K, respectively. Thermal conductivities of $163 \text{ W}\cdot\text{m}^{-1}\cdot\text{K}^{-1}$, $1.2 \text{ W}\cdot\text{m}^{-1}\cdot\text{K}^{-1}$ and $0.1627 \text{ W}\cdot\text{m}^{-1}\cdot\text{K}^{-1}$ were used for silicon, Borofloat and DMC respectively. $Q_{DMC} = 30 \mu\text{l}/\text{min}$ was used at the inlet. DMC properties were chosen according to the reported values by Tundo *et al.*⁵ A direct

linear solver (MUMPS) was employed to obtain the convergent steady-state temperature distribution. The temperature profile along the center of the microchannel at a location immediately after the T-junction is plotted in Fig. S4b.

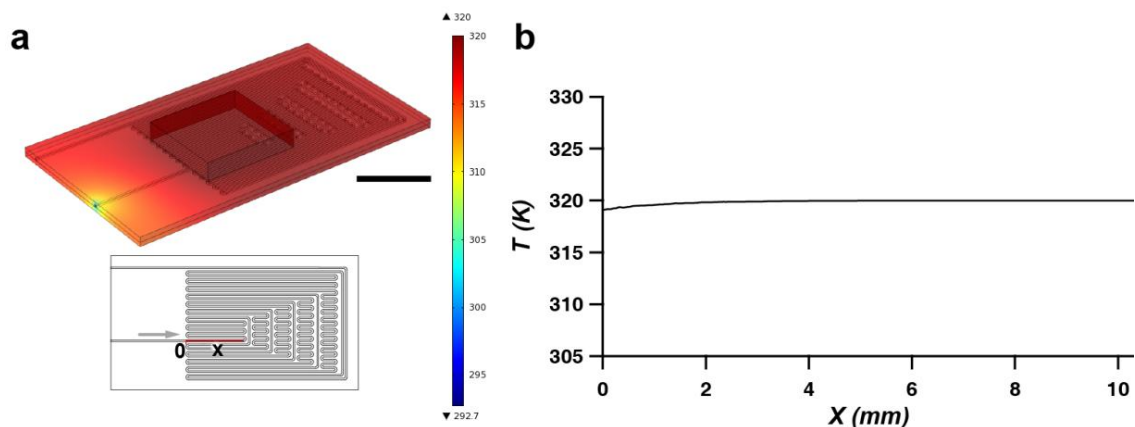


Fig. S4 (a) 3D temperature distribution of the microfluidic system, using a peltier-based heating element attached to the silicon side. Scale bar is 10 mm. (b) Temperature profile along the highlighted red line after the T-junction at the middle of the microchannel.

As shown in Fig. S4b, the temperature of DMC inside the microchannel reached the uniform target temperature of the associated with the segmented flow section of the silicon device prior to entering the T-junction.

S5 Segmented flow of CO₂-DMC at different temperatures

As the Henry's constant for each gas-liquid pair is a function of temperature and pressure, the segmented flow images of CO₂-DMC that are shown at three different temperatures and a fixed DMC flowrate, and CO₂ inlet pressure in Fig. S5 display the effect of the increasing temperature on CO₂ plug dissolution. It can be seen that by increasing temperature, the volume of dissolved CO₂ plugs decreases.

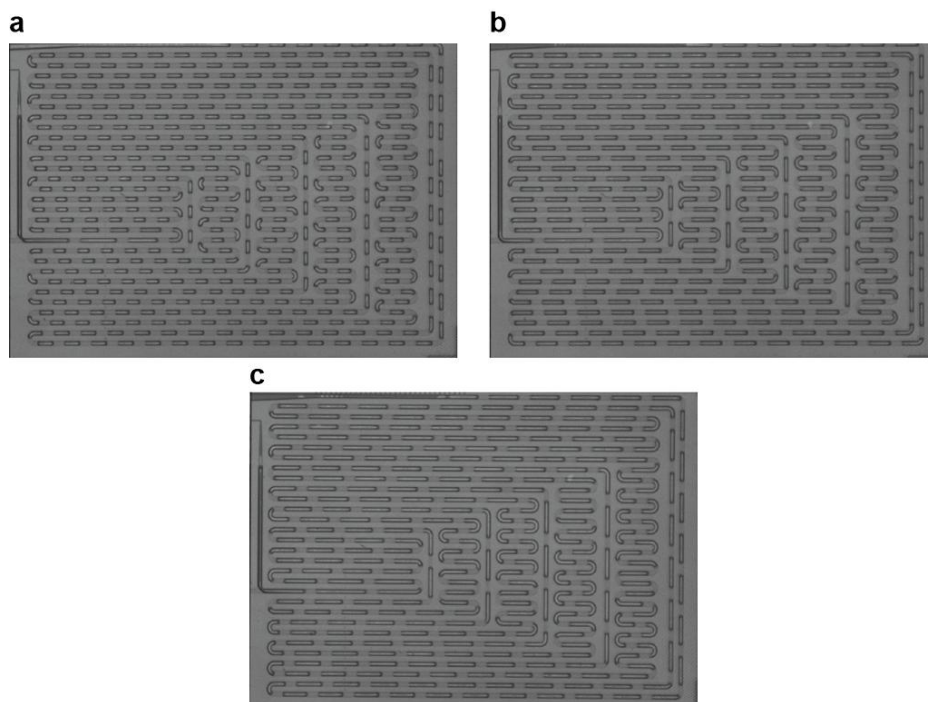


Fig. S5 Regular segmented flow images of CO₂-DMC for three different temperatures. (a) T=299 K, (b) T=301 K, and (c) T=308 K. $j_L=9.26$ mm/s, $P_G=130$ kPa.

S6 Pressure drop calculations

To estimate the plug volume expansion due to the pressure decrease along the flow direction, the pressure drop correlation proposed by Kreutzer *et al.*^{9,10} was used:

$$\frac{\Delta P}{X} = \beta_L f_{slug} \left(\frac{2\rho U_B^2}{D_h} \right), \quad (8)$$

$$f_{slug} = \frac{16}{\text{Re}} \left[1 + 0.17 \frac{w}{L_S} \left(\frac{\text{Re}}{Ca} \right)^{0.33} \right], \quad (9)$$

$$P_0 V_0 = P V_B, \quad (10)$$

where ΔP is the pressure drop along the microchannel, β_L is the total liquid volume fraction in the microchannel, f_{slug} is the friction factor for a segmented flow, Re is Reynolds number, Ca is Capillary number and ρ is the liquid density. Using Eqs.8-10, the pressure drop and the plug volume expansion along the microreactor for $j_L=7.4$ mm/s, $P_G=130$ kPa, and $U_B=63$ mm/s are calculated and plotted in Figs. S6a and b.

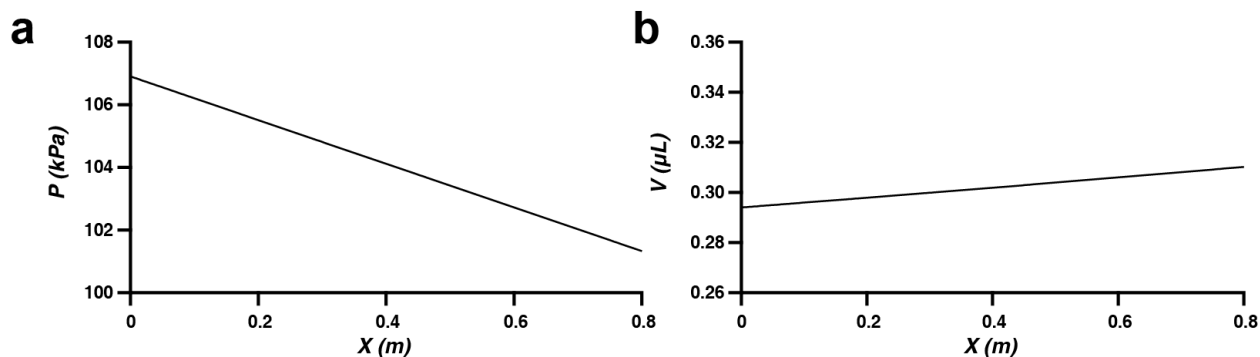


Fig. S6 (a) Pressure drop along the microchannel for $f_{slug}=1.13$ and $\beta_L=0.28$. (b) Plug volume expansion due to the pressure drop. The initial plug length was 3.85 mm.

S7 Microfabrication

The process flow for the fabrication of the designed silicon-based MF device, implemented the shadow mask (nested mask¹¹) process. The process flow is shown in Fig. S7 and started with wafer cleaning (RCA1) and thermal growth of a 1 μm thick oxide layer. A thin resist (Microposit S1813, Shipley Company, Marlborough, MA, USA) was used to pattern the front oxide layer for the pressure drop channels (75 μm deep). The thin resist was removed (Piranha), and a thick resist (AZ9245, Clariant Corporation, Somerville, NJ, USA) was spin coated and patterned for the deep microchannels (300 μm). The oxide layer was then etched using buffered oxide etchant (BOE). At this point of the process, two masks were placed on top of each other (nested mask), the deep channel patterns on the oxide layer were opened, and the shallow channel patterns were covered by the thick positive resist. The lithographically patterned silicon wafer was placed in the deep reactive ion etching (DRIE) chamber (Tegal SDE1100, Tegal Corporation, Petaluma, CA, USA), and the deep features were etched for 225 μm . The thick resist layer was then removed inside the DRIE chamber using oxygen plasma cleaning for 5 min. By removing the thick resist layer, the shallow channel patterns were exposed. DRIE was continued for 75 μm to etch the shallow microchannels, and finish etching of the deep microchannels.

The oxide layer was removed and a new 1 μm oxide was grown on both sides of the patterned silicon wafer. A thick resist was spin coated on the back side of the wafer and a thin resist layer was used to protect the etched front side of the wafer during BOE. The inlet and outlet holes were patterned on the back side. Using DRIE, the back side of the silicon wafer was etched 350 μm , and inlet and outlet holes were connected to the front side.

The oxide layer was removed using BOE, and a fresh 500 nm oxide layer was grown on the finalized silicon wafer for oxidation. The wafers were then anodically bonded to a 6" Borofloat 33 wafer on wafer level. Individual microfluidic devices were isolated from the wafer using a die saw.

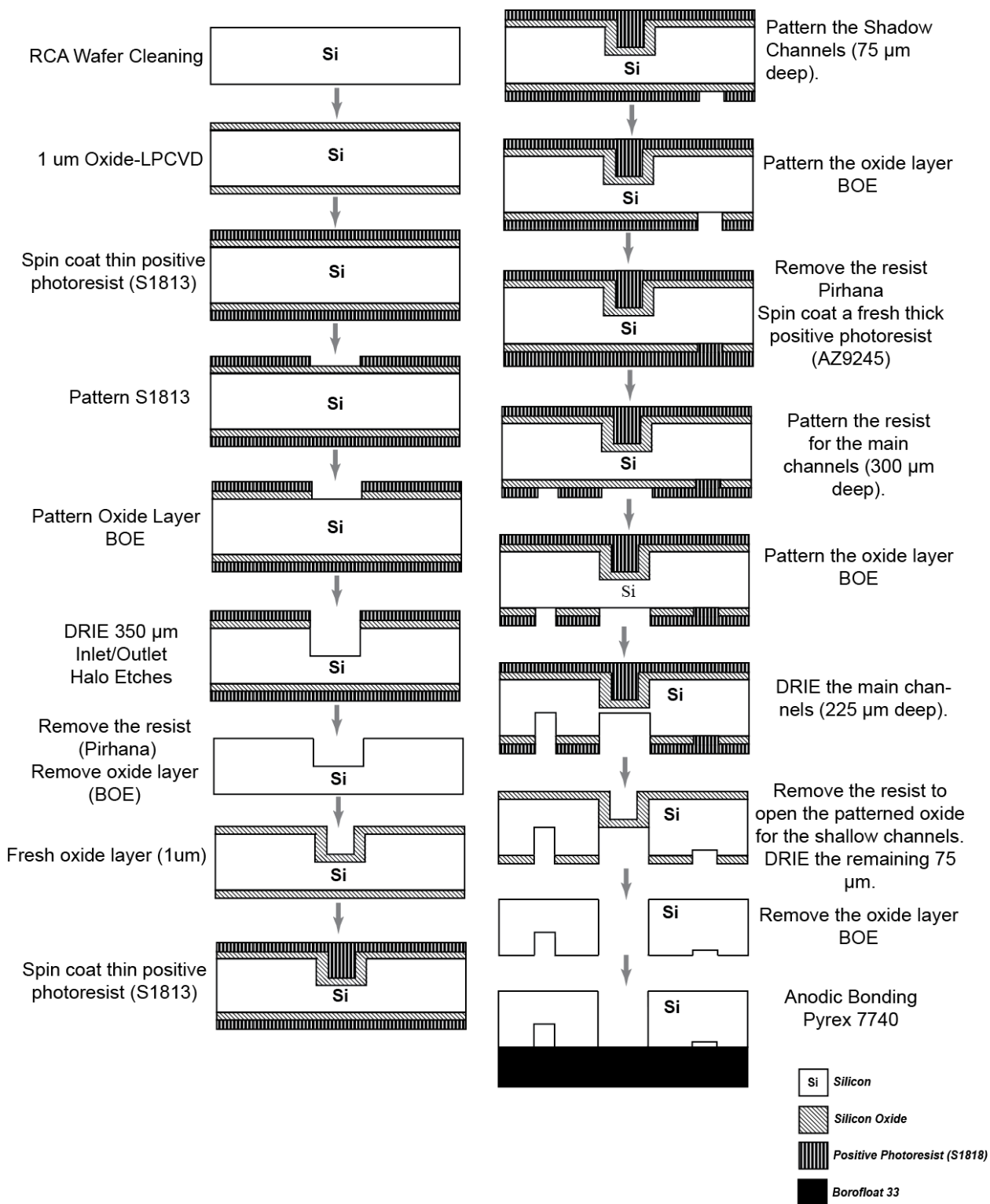


Fig. S7 Process flow for the fabrication of silicon-based MF devices.

S8 CO₂ plug shrinkage (Fig. 6a)

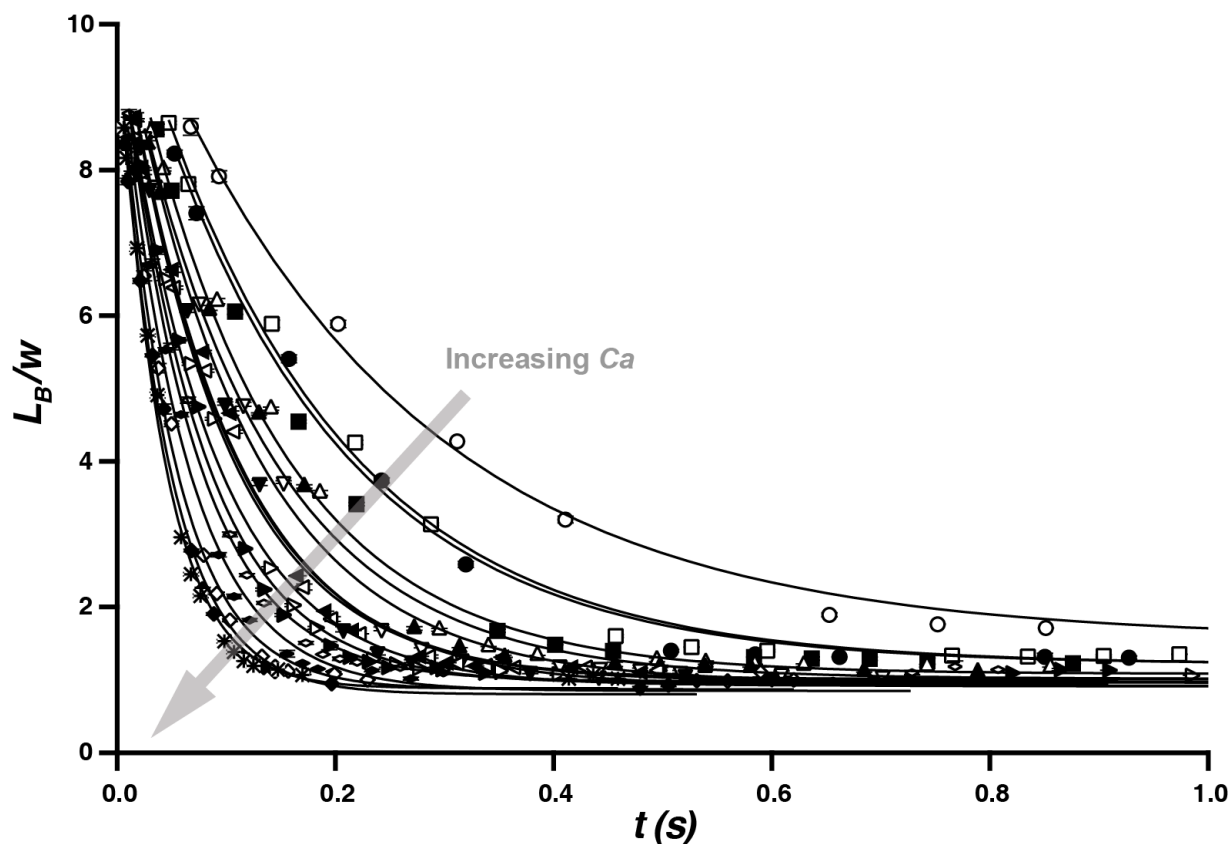


Fig. S8 Carbon dioxide plug evolutions measured at six locations along the flow direction for a constant initial plug length, 2.55 mm, and variable initial plug velocities. Experimental conditions are: $j_L = 5.55$ mm/s, $P_G = 118$ kPa and $U_B = 25.2$ mm/s (\circ); $j_L = 7.4$ mm/s, $P_G = 120$ kPa and $U_B = 32.4$ mm/s (\bullet); $j_L = 9.3$ mm/s, $P_G = 123$ kPa and $U_B = 36$ mm/s (\square); $j_L = 11.1$ mm/s, $P_G = 127$ kPa and $U_B = 47.2$ mm/s (\blacksquare); $j_L = 12.9$ mm/s, $P_G = 129.6$ kPa and $U_B = 55.7$ mm/s (\triangle); $j_L = 14.8$ mm/s, $P_G = 133$ kPa and $U_B = 60.4$ mm/s (\blacktriangle); $j_L = 16.4$ mm/s, $P_G = 135$ kPa and $U_B = 67.9$ mm/s (∇); $j_L = 18.4$ mm/s, $P_G = 138$ kPa and $U_B = 79.4$ mm/s (\blacktriangledown); $j_L = 20.4$ mm/s, $P_G = 145$ kPa and $U_B = 96$ mm/s (\triangleleft); $j_L = 22.2$ mm/s, $P_G = 148$ kPa and $U_B = 99$ mm/s (\blacktriangleleft); $j_L = 25.9$ mm/s, $P_G = 154$ kPa and $U_B = 118$ mm/s (\triangleright); $j_L = 29.6$ mm/s, $P_G = 162$ kPa and $U_B = 142$ mm/s (\blacktriangleright); $j_L = 33.3$ mm/s, $P_G = 166$ kPa and $U_B = 160$ mm/s (\diamond); $j_L = 37.0$ mm/s, $P_G = 170$ kPa and $U_B = 177$ mm/s (\blacklozenge); $j_L = 40.7$ mm/s, $P_G = 174$ kPa and $U_B = 208$ mm/s (\diamond); $j_L = 46.3$ mm/s, $P_G = 184$ kPa and $U_B = 242$ mm/s (\blacklozenge); $j_L = 51.9$ mm/s, $P_G = 194$ kPa and $U_B = 281$ mm/s ($*$).

S9 Sources of uncertainties in the solubility data

The gas dissolution at the front cap is a source of systematic error in the Henry's constant measurement. Assuming purely diffusive transport during the dissolution and a saturated concentration boundary layer around the cap, the penetration depth, d_{cap} , can be estimated as:

$$d_{cap} = \sqrt{t_{breakup} \times D_{CO_2,DMC}} = \sqrt{\left(\frac{4 \text{ mm}}{20 \text{ mm/s}}\right) \times 2.75 \times 10^{-9} \text{ m}^2/\text{s}} = 2.35 \times 10^{-5} \text{ m} = 23.5 \text{ } \mu\text{m} \quad (11)$$

where $t_{breakup}$ is the gas plug break up time. The volume of liquid contained within the calculated penetration depth is 2.13×10^{-11} L. Considering Henry's law and the mole fraction of dissolved gas, defined as $x = n_g / (n_g + n_l)$, $n_g = 2.53 \times 10^{-10}$ moles of CO₂ are dissolved in the liquid, resulting in a 0.04 % error in determining Henry's constant. The accuracy of the digital pressure regulator and the temperature controllers were 0.5%, and 0.1%, respectively. For the pixel size of the CCD camera (4.86 μm) translating to a distance of 7 μm in the object plane, at least 2 pixels (14 μm) were required to detect an interface by the Matlab-based image processing code. For a 5mm long plug, the uncertainty in measuring L_B was 0.28 %. The accuracy of the 300 μm wide channel, with a chrome resolution of 0.5 μm for lithography, was 0.16%. The channel depth variation after the DRIE etch was ± 2 μm , resulting in a 0.66 % error for the 300 μm deep channel.

$$L_B(1 \pm 0.28\%) \times H(1 \pm 0.66\%) \times W(1 \pm 0.16\%) = V_B(1 \pm 1.1\%) \equiv V_S(1 \pm 1.1\%),$$

$$\frac{P \pm (1 + 0.5\%) \times V_B(1 \pm 1.1\%)}{RT(1 \pm 0.1\%)} = n_g \pm 1.7\%, \quad \frac{\rho \times V_S(1 \pm 1.1\%)}{M_{DMC}} = n_l(1 \pm 1.1\%),$$

$$\frac{n_g(1 \pm 1.7\%)}{n_g(1 \pm 1.7\%) + n_l(1 \pm 1.1\%)} = \frac{n_g(1 \pm 1.7\%)}{(n_g + n_l)(1 \pm 1.11\%)} = x(1 \pm 2.81\%), \quad K_H = \frac{P}{x} \rightarrow \frac{P(1 \pm 0.5\%)}{x(1 \pm 2.81\%)} = K_H(1 \pm 3.31\%).$$

Considering all the aforementioned uncertainties, we estimate the total systematic experimental error to be approximately 3.3 %.

Video S10. Video of carbon dioxide dissolving into DMC in the microfabricated silicon-based MF device. The entire MF device is shown here. $j_L=4.63$ mm/s, $P_G=117$ kPa, and $T=299$ K.

Video S11. Video of the field of view that was used for solubility measurement and mass transfer characterization of carbon dioxide dissolving into DMC. $j_L=5.55$ mm/s, $P_G=114$ kPa, and $T=299$ K.

S12 Experimental Setup

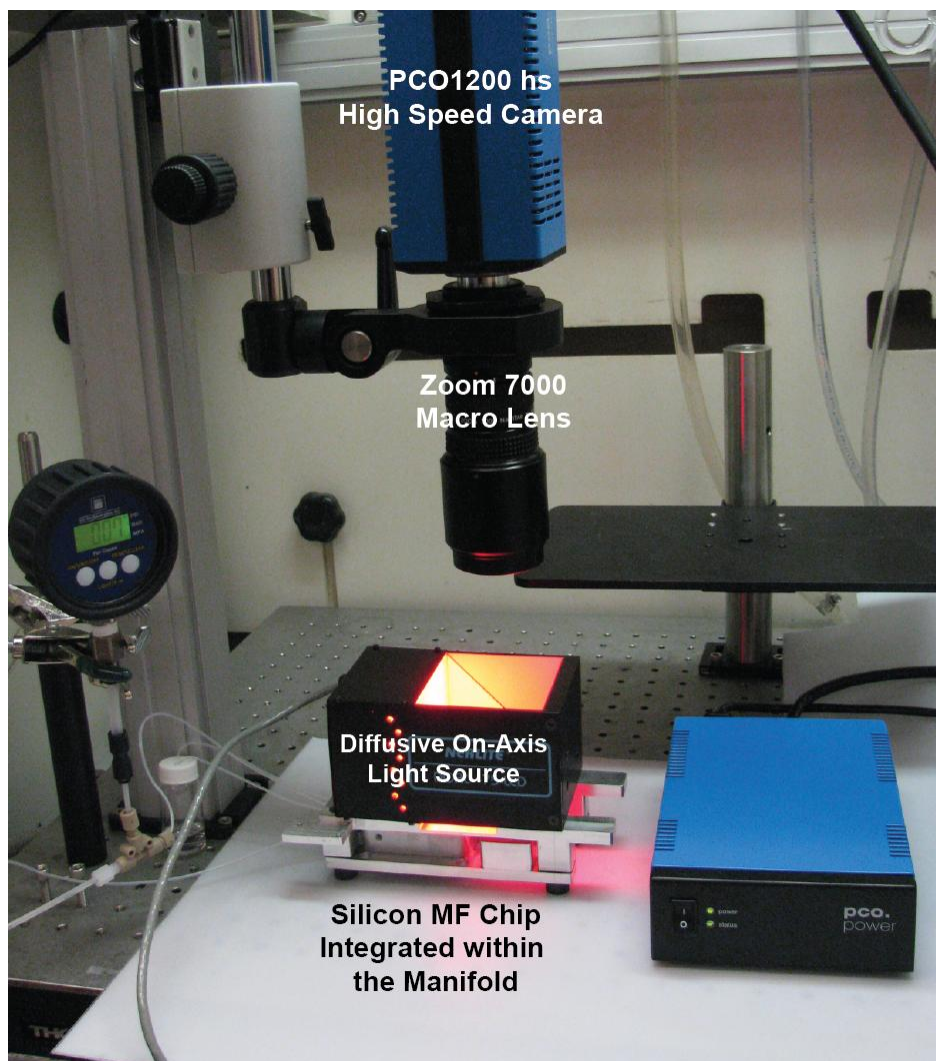


Fig. S12 Experimental Setup.

Supplementary References

1. W. B. Kolb and R. L. Cerro, *Chemical Engineering Science*, 1991, **46**, 2181-2195.
2. D. M. Fries, F. Trachsel and P. R. von Rohr, *International Journal of Multiphase Flow*, 2008, **34**, 1108-1118.
3. G. Versteeg and W. P. M. van Swaaij, *Chemical Engineering Science*, 1988, **43**, 587-591.
4. G. F. Versteeg and W. Van Swaalj, *Journal of Chemical and Engineering Data*, 1988, **33**, 29-34.
5. P. Tundo and M. Selva, *Accounts of chemical Research*, 2002, **35**, 706-716.
6. A. Tamimi, E. B. Rinker and O. C. Sandall, *Journal of Chemical and Engineering Data*, 1994, **39**, 330-332.
7. R. Sun and T. Cubaud, *Lab Chip*, 2011, **11**, 2924-2928.
8. P. Garstecki, M. J. Fuerstman, H. A. Stone and G. M. Whitesides, *Lab Chip*, 2006, **6**, 437-446.
9. M. T. Kreutzer, F. Kapteijn, J. A. Moulijn, C. R. Kleijn and J. J. Heiszwolf, *Aiche Journal*, 2005, **51**, 2428-2440.
10. M. T. Kreutzer, M. G. van der Eijnden, F. Kapteijn, J. A. Moulijn and J. J. Heiszwolf, *Catalysis Today*, 2005, **105**, 667-672.
11. G. Burger, E. Smulders, J. Berenschot, T. Lammerink, J. Fluitman and S. Imai, *Sensors and Actuators A: Physical*, 1996, **54**, 669-673.